



**HAL**  
open science

## **Influence of activation conditions on textural properties and performance of activated biochars for pyrolysis vapors upgrading**

Christian Di Stasi, Gianluca Greco, Rafael Luan Sehn Canevesi, M. Teresa Izquierdo, Vanessa Fierro, Alain Celzard, Belen Gonzalez, Joan Manyà

### **► To cite this version:**

Christian Di Stasi, Gianluca Greco, Rafael Luan Sehn Canevesi, M. Teresa Izquierdo, Vanessa Fierro, et al.. Influence of activation conditions on textural properties and performance of activated biochars for pyrolysis vapors upgrading. *Fuel*, 2020, pp.119759. 10.1016/j.fuel.2020.119759 . hal-03093129

**HAL Id: hal-03093129**

**<https://hal.univ-lorraine.fr/hal-03093129>**

Submitted on 14 Jan 2021

**HAL** is a multi-disciplinary open access archive for the deposit and dissemination of scientific research documents, whether they are published or not. The documents may come from teaching and research institutions in France or abroad, or from public or private research centers.

L'archive ouverte pluridisciplinaire **HAL**, est destinée au dépôt et à la diffusion de documents scientifiques de niveau recherche, publiés ou non, émanant des établissements d'enseignement et de recherche français ou étrangers, des laboratoires publics ou privés.

1 Influence of activation conditions on textural  
2 properties and performance of activated biochars  
3 for pyrolysis vapors upgrading

4 *Christian Di Stasi<sup>1\*</sup>, Gianluca Greco<sup>1</sup>, Rafael L. S. Canevesi<sup>2</sup>, M. Teresa Izquierdo<sup>3</sup>, Vanessa*  
5 *Fierro<sup>2</sup>, Alain Celzard<sup>2</sup>, Belén González<sup>1</sup>, Joan J. Manyà<sup>1</sup>*

6 <sup>1</sup> Aragón Institute of Engineering Research (I3A), Thermochemical Processes Group,  
7 University of Zaragoza, Technological College of Huesca, Crta. Cuarte s/n, 22071 Huesca,  
8 Spain

9 <sup>2</sup> Université de Lorraine, CNRS, IJL, Épinal, F-88000, France

10 <sup>3</sup> Instituto de Carboquímica (ICB-CSIC), Miguel Luesma Castán 4, Zaragoza, E-50018, Spain

11

12 \* Corresponding author at: Aragón Institute of Engineering Research (I3A), Thermochemical  
13 Processes Group, University of Zaragoza, Technological College of Huesca, Crta. Cuarte s/n,  
14 22071 Huesca, Spain

15 E-mail address: [christiandistasi@unizar.es](mailto:christiandistasi@unizar.es).

16 **ABSTRACT**

17 The main aim of the present study is to provide a comprehensive assessment of the effects of  
18 process activation conditions on the textural properties of the resulting activated carbons,  
19 which were produced from wheat straw-derived biochar through chemical activation (with  
20  $K_2CO_3$  at different pressures and mass impregnation ratios) and physical activation (with  $CO_2$   
21 at different temperatures and pressures). For chemically activated biochars, it was found that  
22 specific surface area and pore size distribution were both only positively affected by  
23 increasing the carbonate loading. However, physically activated biochars produced at the  
24 highest pressure and lowest temperature (1.0 MPa and 700 °C) had the highest surface areas  
25 and widest pore size distributions. The materials with the most appropriate textural properties  
26 were then tested as catalysts for steam and dry reforming of the aqueous phase of pyrolysis  
27 oil. The best catalytic performance (a total gas yield of 74% and a selectivity toward  $H_2$  of  
28 almost 40%) was observed for a physically activated biochar. This good performance was  
29 ascribed to the high availability of  $K^0$  on the catalyst surface, which could effectively  
30 promote the reactions involved in the upgrading process.

31 **Keywords**

32 Biochar; chemical activation;  $K_2CO_3$ ; physical activation; pressure; steam and dry reforming  
33 of pyrolysis oil

34

## 35      **1. Introduction**

36      In recent years, the demand for activated carbons has increased due to their usefulness in a  
37 wide range of different applications such as gas and liquid purification [1], electrochemistry  
38 [2], soil remediation [3] and catalysis [4]. Thanks to their versatility to be adapted to specific  
39 applications, these materials are considered promising candidates to address environmental  
40 issues related to global warming and pollution [5]. Nevertheless, the current main drawback  
41 is that the production of activated carbons is still partly based on fossil fuels, which do not  
42 meet sustainability criteria [6,7]. Hence, much more efforts should be made to produce much  
43 more carbons from biomass. However, the direct conversion of biomass feedstock into the  
44 final product has a low yield. Thus, the production of activated carbons from biochar  
45 produced by slow pyrolysis seems to be more appropriate in terms of scalability, while at the  
46 same time these value-added materials can strengthen the value chain of existing biochar  
47 production systems.

48      In general, pristine biochar has neither a well-developed surface area nor a hierarchical  
49 pore size distribution, which is mainly dominated by narrow pores with a diameter ( $d_p$ ) lower  
50 than 0.7 nm (ultra-micropores). Hence, a subsequent activation step is required to improve  
51 the textural properties of the carbon material. The activation process involves the  
52 development and opening of the porosity of a char using an activation agent. Depending on  
53 the agent used, the procedure can be called chemical or physical activation. Chemical  
54 activation usually involves two steps. First, the biochar is impregnated with an aqueous  
55 solution of the chemical activation agent, or mixed with it in the dry state, and, in a second  
56 step, the blend is heated up to a given temperature at which oxidation, dehydration,  
57 aromatization and crosslinking reactions, among others, occur. Although the most widely  
58 used chemical reagents are KOH [8] and H<sub>3</sub>PO<sub>4</sub> [9], non-hazardous and relatively cheap  
59 alternative compounds such as K<sub>2</sub>CO<sub>3</sub> [10,11] have recently attracted considerable attention.

60 Mai *et al.* [12] have recently reported that activation with potassium carbonate can result in  
61 carbons with a high percentage of structural defects and a well-balanced porosity between  
62 micro- and mesopores.

63 When activation is carried out by exposing the precursor to relatively high temperatures  
64 under an oxidizing atmosphere (e.g., CO<sub>2</sub> [13], H<sub>2</sub>O [14] and O<sub>2</sub> [15]), the process is called  
65 physical activation. Through either physical or chemical activation, it is possible to tune the  
66 textural features of the starting biochar by properly adjusting the activation conditions,  
67 mainly temperature, type and/or concentration of activation agent, as well as pressure. To the  
68 best of our knowledge, although both activation procedures are widely reported in the  
69 literature, a thorough study on the effects that the activation parameters and their possible  
70 interactions have on the textural properties of the resulting activated biochar, has never been  
71 reported so far. Such information could be very helpful to properly establish the most  
72 appropriate operating conditions to produce engineered carbon materials from biomass.

73 One of the most interesting fields of application of activated carbons is the upgrading of  
74 raw pyrolysis vapors, which contain both permanent gases (e.g., CO<sub>2</sub>, CO, CH<sub>4</sub>, and H<sub>2</sub>) and  
75 condensable compounds. The condensable fraction, which is generally called pyrolysis oil or  
76 bio-oil, is a mixture of hundreds of organic compounds (alcohols, ketones, acids, etc.) and  
77 water, and its composition strictly depends on the biomass composition and the pyrolysis  
78 operating conditions [16]. For biochar production systems based on slow pyrolysis,  
79 downstream processes aimed at upgrading pyrolysis vapors are required to avoid undesirable  
80 condensation of organic compounds and to increase simultaneously the quality of the gaseous  
81 product. For this purpose, combined steam and dry reforming of pyrolysis oil is a promising  
82 option [17,18], due to the presence of a relatively high amount of CO<sub>2</sub> and steam in the raw  
83 vapor phase. Heterogeneous catalysts based on transition metals such as Ni [19,20], Co [21],  
84 Pt and Rh [22] can be used to improve the overall conversion and the selectivity of the

85 products. However, the main drawback of these catalysts is that the relatively expensive  
86 active phase can easily be poisoned and/or deactivated by deposition of coke [23]. One  
87 possible solution to reduce the overall cost of the upgrading process is to use activated  
88 biochar as catalyst. Its porous structure and inherent inorganic contents (especially K, Mg and  
89 Ca) could result in a relatively good catalytic activity [24–29]. Furthermore, due to the  
90 presence in the reaction system of H<sub>2</sub>O and CO<sub>2</sub>, the carbonaceous support, as well as coke  
91 deposits, could be continuously partly gasified, thus creating new pores to avoid deactivation.  
92 In addition, the spent biochar can be burned to recover energy [30] or, depending on the  
93 metal loaded on the support, employed as soil conditioner [31].

94 Keeping in mind all the above, the main objective of this study was to perform a  
95 preliminary investigation about the effects of several activation conditions on the textural  
96 properties and the catalytic activity of the resulting activated biochars. To this end, wheat  
97 straw-derived biochar was activated chemically and physically with K<sub>2</sub>CO<sub>3</sub> and CO<sub>2</sub>,  
98 respectively, under different operating conditions. To objectively assess the effect of the  
99 selected operation conditions (temperature and mass ratio K<sub>2</sub>CO<sub>3</sub>/precursor for chemical  
100 activation, and temperature and pressure for CO<sub>2</sub> activation), we implemented two factorial  
101 designs of experiments, with two factors and three replicates at the center point. The specific  
102 surface areas and pore size distributions of the resulting activated biochars were then  
103 evaluated. The most promising activated biochars were finally tested as catalysts for steam  
104 and dry reforming of pyrolysis oil. Their performance was evaluated in terms of conversion  
105 of liquid into gas, product selectivity and resistance to deactivation.

## 106 **2. Experimental Section**

107 This study was divided into two main steps: in the first, we carried out physical and  
108 chemical activations under different process conditions in order to study their influence on  
109 the pore size distribution and specific surface area of the resulting activated biochars; in the

110 second part, the most promising materials were then tested as catalysts in pyrolysis vapors  
111 upgrading experiments. The methodology used in this study is summarized graphically in  
112 Fig. A.1.

## 113 ***2.1. Biochar production***

114 The biochar used in this study was produced by slow pyrolysis of binder-free wheat straw  
115 pellets (9 mm OD and 10–13 mm long). Pyrolysis was carried out at atmospheric pressure in  
116 a fixed bed reactor, which was placed inside a furnace and heated up to 500 °C at an average  
117 heating rate of 5 °C min<sup>-1</sup> and using N<sub>2</sub> as carrier gas. More details on the pyrolysis device  
118 and the experimental procedure are available elsewhere [32]. The resulting biochar (i.e.,  
119 “pristine”) was ground and then thoroughly sieved to obtain particle sizes in the range of  
120 0.212 to 1.41 mm. The pristine biochar was characterized by proximate analysis (performed  
121 in quadruplicate according to ASTM standards D3173 for moisture, D3174 for ash, and  
122 D3175 for volatile matter) and ultimate analysis by means of an elemental analyzer CHN628  
123 from Leco Corporation (USA).

## 124 ***2.2. Activation of pristine biochar***

### 125 *2.2.1. Chemical activation*

126 For chemical activation, the pristine biochar was first impregnated with a 1 mol L<sup>-1</sup>  
127 aqueous solution of K<sub>2</sub>CO<sub>3</sub>. Three K<sub>2</sub>CO<sub>3</sub>: biochar mass impregnation ratios (1:1, 2:1 and  
128 3:1) were achieved by adjusting the volume of solution. The heterogeneous mixture was then  
129 stirred for 2 h at 50 °C, filtered and dried overnight at 110 °C to remove the residual water.  
130 Afterwards, 10 g of the impregnated samples were heated up to 700 °C at a heating rate of 10  
131 °C min<sup>-1</sup>, under an inert atmosphere (N<sub>2</sub>), and at three different values of absolute pressure  
132 (0.10, 0.55 and 1.00 MPa). For this purpose, a tubular fixed bed reactor (made of nickel-  
133 chromium alloy UNS N06600, 28.1 mm ID and 600 mm long) placed in a vertical furnace  
134 (model EVA 12/300 from Carbolite Gero, UK) was used. The relatively low activation

135 temperature was chosen to avoid the evaporation of the metallic potassium derived from the  
136 decomposition of the activation agent and, also, to ensure low activation extensions and  
137 clearly see the potential effects of the studied parameters. On the other hand, the range of  
138 activating pressures was chosen in order to allow this experimental setup to be easily scaled  
139 up, since the involved pressures were not too high (up to 1.0 MPa). A soaking time at the  
140 highest temperature of 60 min was set. The pressure within the reactor was adjusted using a  
141 downstream servo-controlled regulator valve. The gas hourly space velocity (GHSV) at the  
142 activation temperature was estimated to be  $7000 \text{ h}^{-1}$ , considering the pressure applied and a  
143 bed void factor of 0.5. Thus, the mass flow rate of the inlet gas stream ( $\text{N}_2$ ) was properly  
144 adjusted as a function of the selected pressure and the highest temperature to achieve the  
145 aforementioned GHSV value.

146 As a last step, the carbons were rinsed to remove the unreacted reagent and other  
147 impurities from their surface. In this work, two different washing procedures were adopted to  
148 assess possible effects on the resulting surface area and the catalytic activity of the activated  
149 carbons produced. For this purpose, among all the unwashed chemically activated biochars,  
150 four of them were just washed with hot deionized water ( $100 \text{ }^\circ\text{C}$ ), while the seven chemically  
151 activated biochars adopted in the design of experiments were washed with a  $0.25 \text{ mol L}^{-1}$   
152 solution of HCl followed by hot water. Both washing procedures were carried out until  
153 neutral pH. The resulting activated biochars were then dried overnight at  $110 \text{ }^\circ\text{C}$ . The  
154 efficiency of the washing step was evaluated according to the washing yield, calculated from  
155 Eq. 1, in which  $m_c$  and  $m_w$  are the masses of activated carbon before and after the washing  
156 steps, respectively.

$$157 \quad Y_{wash} = \left(1 - \frac{m_c - m_w}{m_c}\right) 100 \quad (1)$$

### 158 2.2.2. Physical activation



159 Physically activated biochars were produced under an atmosphere of pure CO<sub>2</sub> at three  
160 different temperatures(700, 775 and 850 °C), and at three different absolute pressures (0.10,  
161 0.55, and 1.00 MPa). The selected activation temperatures are within the range commonly  
162 reported in the literature, whereas the pressure values were established with the purpose to  
163 compare the properties of resulting activated carbons produced under atmospheric and  
164 moderate pressures. Using the same device described in the previous section, 10 g of pristine  
165 biochar were heated under N<sub>2</sub> atmosphere, at a heating rate of 10 °C min<sup>-1</sup>, until the target  
166 temperature was reached. Then, the gas supply was switched from N<sub>2</sub> to CO<sub>2</sub> at a constant  
167 GHSV of 7000 h<sup>-1</sup>. These conditions were maintained during the time required to reach a  
168 degree of burnout ( $\eta$ , defined as the percentage of mass loss) in the range of 30% to 60%.

### 169 2.2.3. Design of experiments

170 To objectively assess the effects of the activation conditions on the textural properties of  
171 activated biochars, an unreplicated two-level factorial design of experiments (with two  
172 factors and three replicates at the center point) was adopted for both chemical and physical  
173 activations. For chemical activation, the analyzed factors were the absolute pressure and the  
174 impregnation ratio of K<sub>2</sub>CO<sub>3</sub> to raw biochar, whereas in the case of physical activation, the  
175 temperature and the absolute pressure were the studied factors. The structure of the  
176 regression model used in the statistical analysis was the following:

$$177 \quad \hat{y} = \beta_0 + \beta_i A + \beta_j B + \beta_{ij} AB \quad (2)$$

178 where  $A$  and  $B$  corresponded to the assessed factors (normalized values in the range from -1  
179 to 1), whereas  $\beta_0$ ,  $\beta_i$ , and  $\beta_{ij}$  were the intercept, linear, and interaction coefficients,  
180 respectively. The results obtained for the selected response variables ( $y$ ) were analyzed using  
181 the Minitab v17 statistical package. A significance level of 5% was assumed and the adjusted  
182 coefficient of determination ( $R^2_{adj}$ ) was taken as an indicator of the quality of the fit. Table 1  
183 summarizes the adopted designs of experiments and lists the names of the activated biochars

184 produced. Briefly, activated biochar are referred as  $X\_Y\_P$ .  $X$  corresponds to the activation  
185 procedure (CB or PB for *chemically activated biochar* and *physically activated biochar*,  
186 respectively);  $Y$  is the activation temperature for PBs or the impregnation ratio for CBs; and  $P$   
187 is the activation pressure.

### 188 ***2.3. Catalytic pyrolysis vapors upgrading***

189 The liquid feed used here for pyrolysis vapors upgrading tests was the filtered aqueous  
190 phase of the pyrolysis oil formed during the production of pristine biochar derived from  
191 wheat straw. This resulting liquid product was characterized in terms of elemental  
192 composition, using the same CHN analyzer as mentioned in section 2.1, and water content,  
193 using a volumetric Karl-Fischer titrator Titrino plus 870 from Metrohm (Switzerland).

194 A schematic overview of the experimental device used for the reforming tests is shown in  
195 Fig. A.2 (Appendix A). The reactor and furnace elements were the same as those previously  
196 described in section 2.2. The reforming operating conditions were selected based on the  
197 findings of a previous study [33], which aimed to establish the best process conditions to  
198 minimize deactivation by coke deposition.

199 Briefly, activated biochar (2–5 g) was loaded into the reactor and heated under  $N_2$   
200 atmosphere at an absolute pressure slightly above 0.1 MPa. Once the bed temperature  
201 reached the target value of 750 °C,  $CO_2$  was added to the inlet gas stream at a partial  $CO_2$   
202 pressure of 0.02 MPa. The liquid feed was then injected into the gas stream at the inlet of the  
203 reactor by means of a HPLC pump (model 521 from Analytical Scientific Instruments, USA).  
204 The liquid hourly space velocity (LHSV) was kept constant and equal to  $2\text{ h}^{-1}$  for all the  
205 experiments conducted. The duration of the experiments was 60 min. The reactor outlet  
206 stream, consisting of permanent gases, unreacted pyrolysis oil, and condensable side  
207 products, was forced to pass through an ice-bath condensation train. The permanent gases  
208 were analyzed using a dual-channel micro gas chromatograph ( $\mu$ -GC 490 from Agilent,

209 USA) equipped with TCD detectors and two analytical columns (a Molsieve 5 A and a  
 210 PolarPlot U). The known amount of N<sub>2</sub> fed was used as a tracking compound to calculate the  
 211 yield of produced gas.

212 **Table 1.** Matrix of the factorial designs adopted to assess the effects of the selected factors  
 213 during both chemical and physical activations. For example, a physical activation carried out  
 214 at A=-1 and B=1 means that the process was performed at 700°C and 1.0 MPa

<b>Chemical activation</b>			
(thermal treatment under N <sub>2</sub> up to 700 °C and 1 h soaking time)			
<b>Level</b>	<b>Factors</b>		<b>Response Variables</b>
	A Pressure (MPa)	B Mass ratio (K <sub>2</sub> CO <sub>3</sub> : raw biochar)	<i>S<sub>2D-NLDFT</sub>, V<sub>b</sub>, V<sub>ultra</sub>, V<sub>micro</sub>, V<sub>meso</sub></i>
Low (-1)	0.10	1:1	
Middle (0)	0.55	2:1	
High (+1)	1.00	3:1	
<b>Runs</b>			<b>Activated biochar designation</b> (all washed with an acidic solution)
1	0	0	CB_2_0.55
2	-1	+1	CB_3_0.10
3	+1	+1	CB_3_1.00
4	0	0	CB_2_0.55
5	0	0	CB_2_0.55
6	-1	-1	CB_1_0.10
7	+1	-1	CB_1_1.00
<b>Physical activation</b>			
<b>Level</b>	<b>Factors</b>		<b>Response Variables</b>
	A Temperature (°C)	B Pressure (MPa)	<i>S<sub>2D-NLDFT</sub>, V<sub>b</sub>, V<sub>ultra</sub>, V<sub>micro</sub>, V<sub>meso</sub></i>
Low (-1)	700	0.10	
Middle (0)	775	0.55	
High (+1)	850	1.00	
<b>Runs</b>			<b>Activated biochar designation</b>
1	-1	-1	PB_700_0.10
2	-1	+1	PB_700_1.00
3	+1	+1	PB_850_1.00
4	0	0	PB_775_0.55
5	0	0	PB_775_0.55
6	+1	-1	PB_850_0.10
7	0	0	PB_775_0.55

215

216

217 The performance of the activated biochars tested was measured in terms of total gas yield  
218 ( $Y_g$ ) and hydrogen yield ( $Y_{H_2}$ ), as defined by Eqs. (3) and (4), respectively.

219

$$220 \quad Y_g = \frac{m_g}{m_L} 100 \quad (3)$$

$$221 \quad Y_{H_2} = \frac{F_{H_2,av}}{F_{H_2,stoi}} 100 \quad (4)$$

$$222 \quad F_{H_2,stoi} = \left(2n + \frac{m}{2} - k\right) F_{BO} \quad (5)$$

$$223 \quad S_i = \frac{n_i}{n_{tot}} 100 \quad (6)$$

224 In Eq. (3),  $m_g$  was the cumulative mass of the gas produced during the 60-min  
225 experiments, whereas  $m_L$  corresponded to the total mass of the liquid fed. In Eq. (4),  $F_{H_2,av}$   
226 was the experimental average molar flow rate of hydrogen from minute 20 to minute 40.  
227  $F_{H_2,stoi}$ , which was calculated according to Eq. (5), corresponded to the stoichiometric molar  
228 flow rate of hydrogen considering the contribution from steam reforming reaction.  $F_{BO}$  was  
229 the molar flow rate of the dry pyrolysis oil fed. The selectivity towards specific gaseous  
230 products ( $S_i$ ) was calculated according to Eq. (6), in which  $n_{tot}$  was the sum of the gaseous  
231 products in moles at the outlet stream.

#### 232 **2.4. Characterization of carbon materials**

233 The textural properties of pristine and activated biochars were determined from both N<sub>2</sub>  
234 and CO<sub>2</sub> adsorption isotherms at -196 °C and 0 °C, respectively. Around 120 mg of sample  
235 were degassed under vacuum at 150 °C. ASAP 2020 and ASAP 2420 automatic adsorption  
236 analyzers (Micromeritics, USA) were used. The results obtained from the isotherms were  
237 treated using the MicroActive software. We determined the BET area ( $A_{BET}$ ) by application of  
238 the BET model, as well as the Gurvitch volume ( $V_{0.97}$ ). The enhanced 2D-NLDFT model [34]  
239 was employed using SAIEUS software (available at [www.nldft.com](http://www.nldft.com)) to evaluate the pore size  
240 distributions (PSDs) and other related parameters: surface area ( $S_{2D-NLDFT}$ ), ultra-micropore

241 volume ( $V_{ultra}$ ,  $d_p < 0.7$  nm), micropore volume ( $V_{micro}$ ,  $d_p < 2$  nm), total pore volume ( $V_t$ ) and  
242 mesopore volume ( $V_{meso}$ ,  $d_p$  in the range of 2 to 50 nm). The latter was calculated as the  
243 difference between  $V_t$  and  $V_{micro}$ .

244 To evaluate the availability of residual potassium carbonate on the surface of chemically  
245 activated biochars, Fourier-transform Infrared Spectroscopy (FTIR) analyses were conducted  
246 using a Frontier MIR/NIR Spectrometer from PerkinElmer (USA).

247 Qualitative temperature-programmed desorption (TPD) analyses of pristine biochar and  
248 fresh catalysts used in reforming tests were also performed to assess the thermal stability of  
249 these samples. TPD measurements were carried out using a thermogravimetric analyzer  
250 coupled with a mass spectrometer (STA 449 F3 and QMS 403 Aëolos Quadro from Netzsch,  
251 Germany), by heating the sample up to 750 °C at a heating rate of 5 °C min<sup>-1</sup> under an Ar  
252 atmosphere.

253 A FEI XL30 SFEG scanning electron microscope coupled with energy-dispersive X-ray  
254 spectroscopy (Oxford Instrument EDS SDD XMAX detector) was used to characterize the  
255 surface of fresh and spent activated biochars. The secondary electron images were taken with  
256 an acceleration voltage of 3 or 5 kV to investigate the topology of the samples surface, while  
257 an acceleration tension of 10 kV was applied to carry out the chemical mapping of the  
258 materials by EDX analysis. Additionally, X-ray photoelectron spectroscopy (XPS) data of  
259 spent and fresh catalysts were recorded using an ESCAPlus OMICROM system equipped  
260 with a hemispherical electron energy analyzer, following the procedure detailed elsewhere  
261 [35].

### 262 **3. Results and discussion**

263 The results of the textural characterization as well as the proximate and ultimate analyses  
264 of the pristine biochar are summarized in Table A.1. The reported values of  $A_{BET}$  and  $S_{2D}$ .

265 *NLDFT* confirm that the porosity of the pristine biochar, as previously stated, was characterized  
266 by a very high fraction of ultra-micropores.

### 267 **3.1. Chemical activation**

268 Although the use of  $K_2CO_3$  as catalyst in coal gasification processes has been widely  
269 reported in the literature [10–12,33], the mechanism explaining its interaction with the carbon  
270 matrix still remains unclear. The main reactions that probably occur during chemical  
271 activation of a carbonaceous material are the following:



276 The increase in specific surface area could be ascribed to the  $CO_2$  released from carbonate  
277 decomposition (Reaction 7), which can diffuse into the solid structure and subsequently react  
278 with carbon, thereby stimulating the production of CO by the reverse Boudouard reaction  
279 (Reaction 8) and creating vacancies in the solid structure [36]. Despite the fact that the  
280 decomposition of  $K_2CO_3$  mainly occurs at temperatures above 900 °C, its contact with the  
281 carbon matrix can promote its decomposition at relatively low temperatures [37,38]. The  
282 potassium oxide resulting from the decomposition of the carbonate, or the carbonate itself,  
283 can also react with the carbon-based material through Reaction 9 and 10 towards CO and  
284 metallic potassium [39].

285 The assessed textural properties of chemically activated biochars are listed in Table 2. Fig.  
286 1 shows the normalized plots of the standardized effects for the response variables  
287 considered:  $S_{2D-NLDFT}$ ,  $V_t$ ,  $V_{ultra}$ ,  $V_{micro}$ , and  $V_{meso}$ . The PSDs obtained for biochars activated  
288 with different impregnation ratios and the  $N_2$  adsorption isotherms of such samples are shown

289 in Figs. A.3a and A.4, respectively. More detailed statistical outcomes for the results reported  
290 in the present section can be found in Table A.2.

291

292 **Table 2.** Results of textural characterization and washing efficiency of chemically activated  
 293 biochars

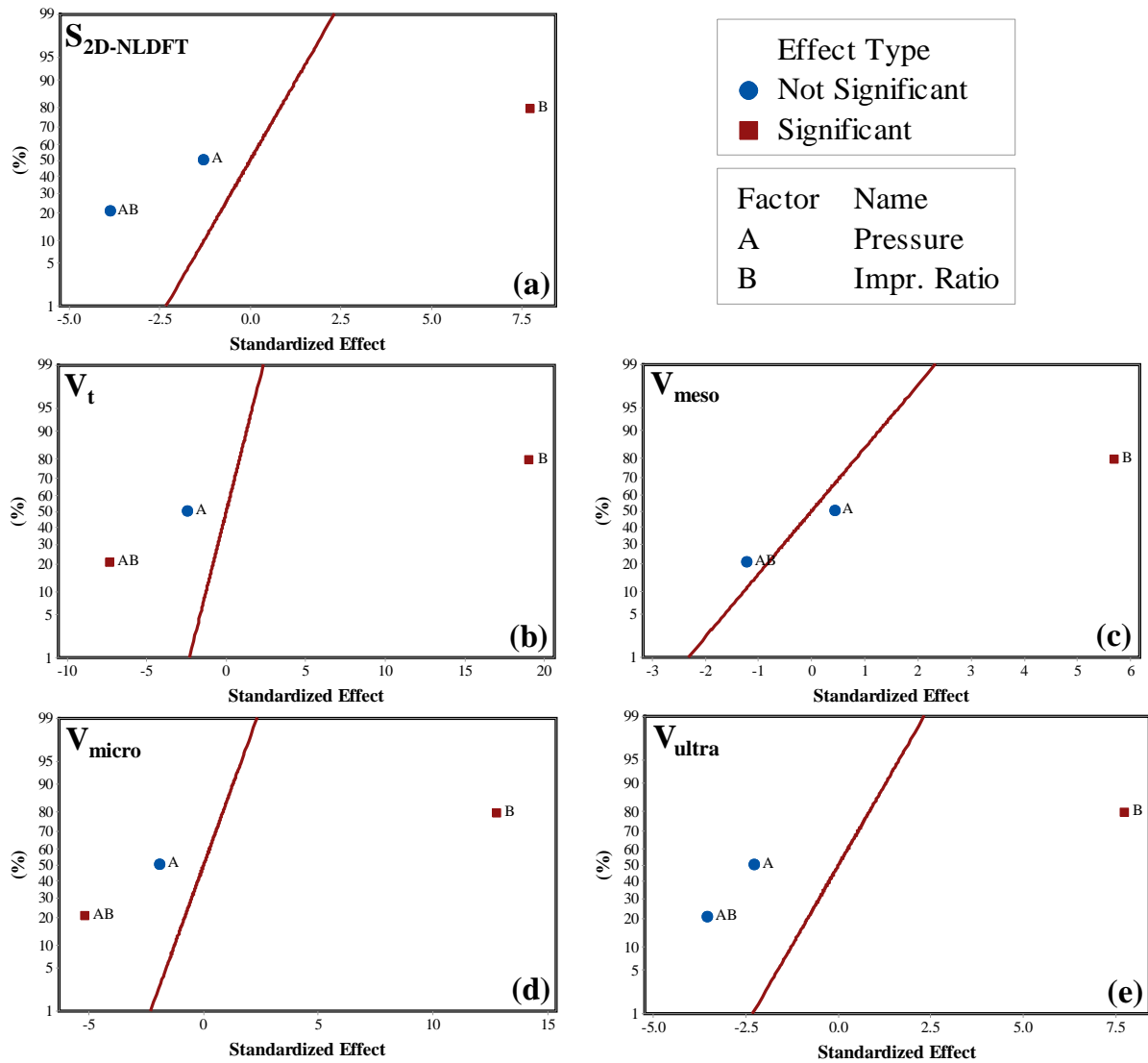
Material	Specific surface area		$V_{0.97}$	$V_t$	Pore volumes			Washing yield $Y_{wash}$ %
	$A_{BET}$	$S_{2D-NLDFT}$ $m^2 g^{-1}$			$V_{ultra}$	$V_{micro}$	$V_{meso}$	
CB_1_0.10	170	712	0.078	0.181	0.143	0.175	0.006 (3.19 %) <sup>a</sup>	77.0
CB_1_0.10_W <sup>b</sup>	142	700	0.068	0.180	0.135	0.169	0.011 (6.14 %) <sup>a</sup>	77.1
CB_1_1.00	180	761	0.081	0.195	0.149	0.188	0.007 (3.82%) <sup>a</sup>	76.4
CB_1_1.00_W <sup>b</sup>	100	700	0.049	0.168	0.144	0.160	0.008 (5.01%) <sup>a</sup>	78.1
CB_3_0.10	413	933	0.181	0.259	0.197	0.246	0.013 (4.96%) <sup>a</sup>	54.3
CB_3_0.10_W <sup>b</sup>	368	893	0.158	0.242	0.193	0.229	0.013 (5.35%) <sup>a</sup>	56.0
CB_3_1.00	337	834	0.148	0.230	0.169	0.218	0.012 (5.23%) <sup>a</sup>	56.9
CB_3_1.00_W <sup>b</sup>	316	851	0.138	0.229	0.180	0.217	0.012 (5.40%) <sup>a</sup>	60.6
CB_2_0.55	316	900	0.137	0.238	0.180	0.228	0.009 (3.92%) <sup>a</sup>	58.1
CB_2_0.55	310	872	0.136	0.233	0.177	0.222	0.011 (4.63%) <sup>a</sup>	54.4
CB_2_0.55	307	864	0.137	0.233	0.171	0.221	0.011 (4.86%) <sup>a</sup>	55.5

294 <sup>a</sup> Calculated as  $\frac{V_{meso}}{V_t} 100$

295 <sup>b</sup> Carbons just washed with water that were not included in the design of experiments.

296





297 **Fig. 1.** Normal plots of standardized effects ( $\alpha = 0.05$ ) for chemically activated biochars:  
 298 specific surface area (a); total pore volume (b); mesopore volume (c); micropore volume (d);  
 299 ultra-micropore volume (e).

300 Regarding the results obtained in terms of specific surface area ( $S_{2D-NLDFT}$ ), Fig. 1a clearly  
 301 shows that a higher concentration of activation agent led to a significant increase in the  
 302 porosity of the resulting activated biochars. In contrast, the absolute pressure proved to be  
 303 irrelevant for the values of final specific surface area. Our results regarding the development  
 304 of porosity when higher impregnation ratios were used confirm the relevance of  $K_2CO_3$  as a  
 305 chemical reagent for the production of tailored activated carbons. All pore volumes analyzed  
 306 in the present study were also found to be strongly dependent on the amount of activating

307 agent (see Fig. 1). The chemical activation process was able to slightly broaden the original  
308 pore size distribution of the pristine biochar, leading to a more hierarchical porous structure  
309 with a large contribution of ultra-micropores and a slightly increased amount of mesopores.  
310 Almost all the carried out  $N_2$  isotherms required more than 70 h to be completed, thus  
311 confirming the predominant narrow microporous structure of chemically activated biochars  
312 (see Fig. A.3a), which hindered the diffusion of  $N_2$  within the porosity. For both total and  
313 micropore volumes, a statistically significant combined effect of pressure and impregnation  
314 ratio (AB) was found. However, these effects were comparatively much weaker than that  
315 observed for the main effect of the impregnation ratio (B). From a thermodynamics point of  
316 view, an increased pressure shifts the equilibrium of the activation reactions to the left. The  
317 fact that the textural properties of the resulting activated carbons were practically  
318 independent of pressure could indicate that the chemical activation process was mainly  
319 kinetically controlled.

320 It should be pointed out that the overall curvature terms for  $S_{2D-NLDFT}$ ,  $V_t$  and  $V_{micro}$  were  
321 statistically significant ( $p$ -values below 0.05, as reported in Table A.2). This indicates that, in  
322 further studies, our adopted factorial design should be expanded to a central composite design  
323 to be able to evaluate the pure quadratic regression coefficients and then apply Response  
324 Surface Methodology (RSM) for optimization purposes.

325 As shown in Table 2, after the carbons were washed only with hot water, there was a  
326 slight decrease in both the specific surface area and the micropore volume, compared to those  
327 measured for carbons washed with the acidic solution. This can be explained by the fact that  
328 water could not completely remove the remaining carbonate (and other chemical species)  
329 from the solid surface, thus causing blockage of some micropores. By focusing on the  
330 difference between the washing procedures of activated carbons at the same loadings of  
331  $K_2CO_3$ , the results reported in Table 2 indicate that a higher activation pressure led to an

332 increased amount of product not soluble in water, i.e., to higher  $Y_{wash}$  values. This finding  
333 agrees with results reported by Malekshahian *et al.* [40], who concluded that high gasification  
334 pressures can limit the volatilization of potassium.

### 335 **3.2. Physical activation**

336 It must be pointed out that an increase in absolute pressure also implied an increase in the  
337 partial pressure of the reactant ( $\text{CO}_2$ ). In the literature, the effects of absolute pressure and  
338 partial pressure of reactant are commonly assessed separately. Nevertheless, and as far as we  
339 know, no previous studies have addressed the question of whether activation under pressure  
340 can cause textural changes in the resulting physically activated biochars. Activation of  
341 biomass-derived carbon had only been studied using supercritical water at high pressure [41],  
342 but such conditions are too different from the present ones for allowing some comparison to  
343 be done.

344 Table 3 lists the textural properties of the activated carbons produced, whereas Fig. 2  
345 shows the normal plots of the standardized effects obtained for each response variable. More  
346 detailed statistical outcomes are reported in Table A.3. The most relevant PSDs and  $\text{N}_2$   
347 adsorption isotherms are shown in Figs. A.3b and A.5, respectively. As previously mentioned  
348 in section 2.2.2, the activation times (also shown in Table 3) were varied to obtain degrees of  
349 burnout in the range of 30% to 60 %, since the gasification rate was strictly dependent on  
350 reaction temperature and reactant partial pressure. As expected, the reaction rate was minimal  
351 at the lowest temperature (700 °C). In fact, and whatever the pressure applied, an activation  
352 time of 180 min was required to reach the desired reaction extent. For activation temperatures  
353 of 775 and 850 °C, an activation time of 60 min was enough, except for the material  
354 PB\_850\_1.00, for which this reaction time led to an almost complete gasification of the  
355 sample ( $\eta = 85\%$ ). Hence, the activation time at the highest levels of temperature and  
356 pressure was finally set at 30 min to obtain a degree of burnout of 57%.

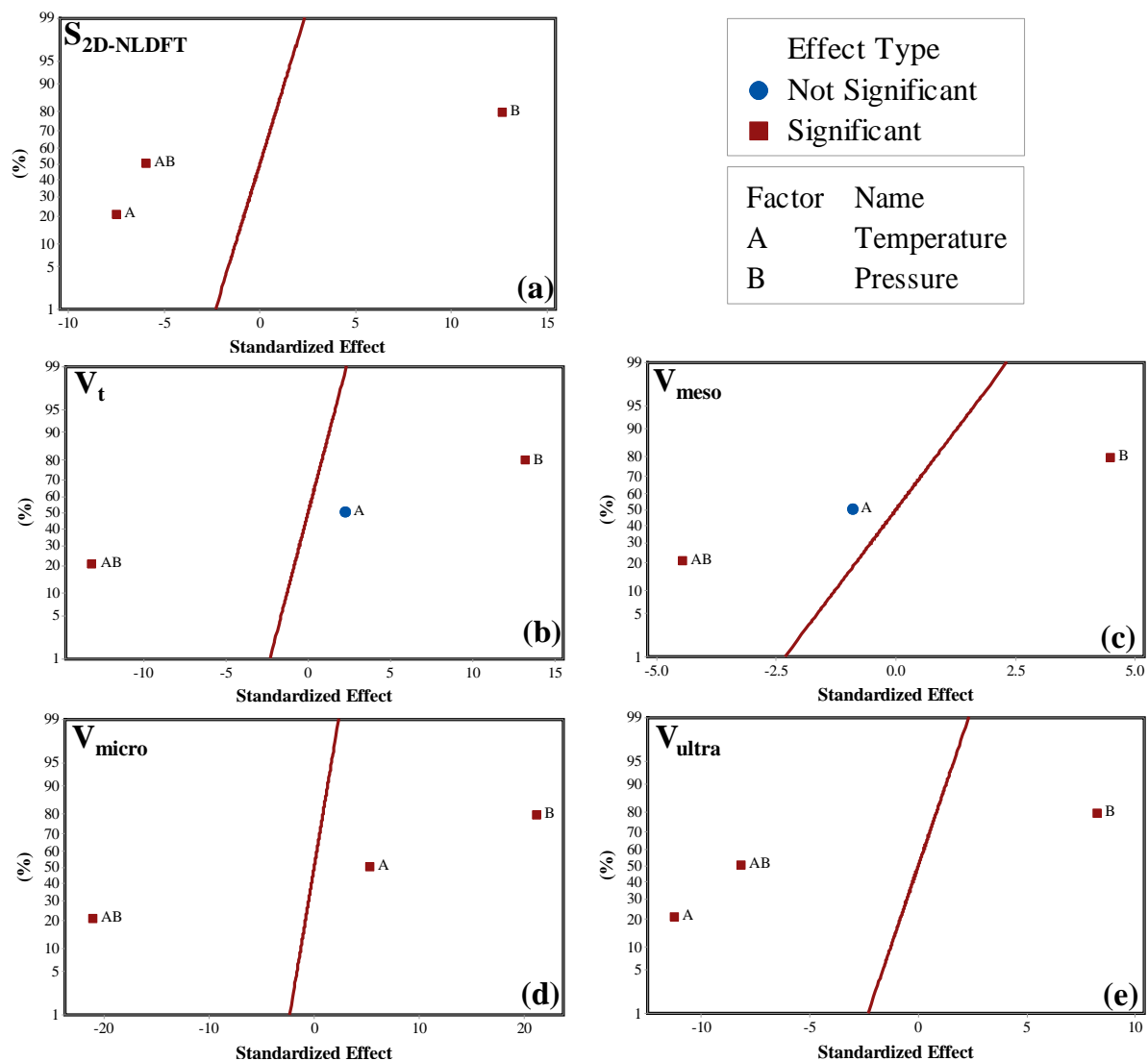
357 **Table 3.** Degrees of burnout activation times and textural properties for physically activated  
 358 biochars

Material	Activation time	Burnout $\eta$ %	Specific surface area		Pore volumes				
	$t_{act}$ min		$A_{BET}$	$S_{2D-NLDFT}$ $m^2 g^{-1}$	$V_{0.97}$	$V_t$	$V_{ultra}$	$V_{micro}$ $cm^3 g^{-1}$	$V_{meso}$
PB_700_0.10	180	30.1	552	833	0.237	0.243	0.184	0.227	0.016 (6.77%) <sup>c</sup>
PB_700_1.00	180	52.8	743	1008	0.333	0.333	0.226	0.301	0.032 (9.55%) <sup>c</sup>
PB_850_0.10	60	54.9	600	818	0.263	0.266	0.169	0.240	0.026 (9.64%) <sup>c</sup>
PB_850_1.00	30	56.7	688	881	0.298	0.296	0.176	0.273	0.022 (7.57%) <sup>c</sup>
PB_775_0.50	60	43.7	719	931	0.314	0.312	0.176	0.285	0.027 (8.62%) <sup>c</sup>
PB_775_0.50	60	42.2	707	936	0.309	0.306	0.171	0.282	0.025 (8.02%) <sup>c</sup>
PB_775_0.50	60	42.4	707	949	0.308	0.306	0.174	0.282	0.023 (7.64%) <sup>c</sup>
PB_650_0.10 <sup>d</sup>	60	12.5	68.8	482	0.029	0.126	0.100	0.124	0.001 (1.07%) <sup>c</sup>
PB_650_1.00 <sup>d</sup>	180	25.0	447	750	0.191	0.214	0.154	0.200	0.014 (6.46%) <sup>c</sup>

359 <sup>c</sup> Calculated as  $\frac{V_{meso}}{V_t} 100$

360 <sup>d</sup> Additional carbons that were not included in the design of experiments.

361 It was clear that a high pressure accelerated carbon gasification, even at 700 °C. At this  
 362 temperature, an increase in pressure from 0.1 to 1.0 MPa led to a marked increase in the  
 363 burnout, from 30.1% to 52.8%, due to the higher reaction rate. In this sense, an increased  
 364 CO<sub>2</sub> partial pressure resulted in a higher fraction of reactant adsorbed on the surface of the  
 365 sample [42]. These outcomes are in agreement with the study conducted by Malekshahian *et*  
 366 *al.* [42], but disagree with the results reported by Feroso *et al.* [43], who observed that  
 367 gasification of heartwood was enhanced using low partial pressures of CO<sub>2</sub>.



368 **Fig. 2.** Normal plots of standardized effects ( $\alpha = 0.05$ ) for physically activated biochars:  
 369 specific surface area (a); total pore volume (b); mesopore volume (c); micropore volume (d);  
 370 ultra-micropore volume (e).

371 The specific surface areas reported in Table 3 were in line with expectations, given the  
 372 present activation conditions. Even at the lowest temperatures (700 °C) it was possible to  
 373 obtain relatively high surface areas, even greater than those measured for activated biochars  
 374 produced at higher temperatures. As can be seen in Fig. 2a, the specific surface area was  
 375 positively influenced by the absolute pressure and negatively affected by the activation  
 376 temperature. Especially at 1.0 MPa, relatively low temperatures and longer activation times  
 377 allowed the biochar to be gasified more homogeneously, thus resulting in a more developed

378 porous structure. Conversely, higher temperatures led to faster reaction rates, which can  
379 result in a more severe enlargement of micropores and the subsequent loss of surface area.

380 Fig. 2b shows that the total pore volume increased significantly when the pressure was  
381 raised from 0.1 to 1.0 MPa. In general, the total pore volumes for physically activated  
382 biochars, which were not significantly affected by the activation temperature, were higher  
383 than those measured for chemically activated carbons. As can be seen when comparing the  
384 data reported in Tables 2 and 3, physical activation led to porous carbons with slightly higher  
385 ultra-micropore volumes. An inspection of Figs. 2d, 2e and A.3b reveals that high  
386 temperatures can lead to some widening of the narrowest micropores, since the activation  
387 temperature had a negative effect on the ultra-micropore volumes and a positive one on the  
388 micropore volumes. With regards to the volume of mesopores, which was mainly affected by  
389 pressure (see Fig. 2c), it should be noticed that physical activation under pressure resulted in  
390 more hierarchical porous structures with higher contributions of mesopores (see values of  
391  $V_{meso}$  and relative percentages in Table 3). The statistically significant overall curvature terms  
392 reported in Table A.3 for  $S_{2D-NLDFIT}$ ,  $V_t$ ,  $V_{meso}$ , and  $V_{micro}$  response variables also suggest that a  
393 central composite design could be required for optimization purposes.

394 Given the significant effects of pressure on the textural properties of carbons activated at  
395 700–850 °C, we decided to perform two additional physical activations at 650 °C, leading to  
396 the materials called PB\_650\_0.10 and PB\_650\_1.00. The results obtained, which are also  
397 reported in Table 3, seem to confirm that activation with CO<sub>2</sub> under pressure is a very  
398 interesting way to produce biomass-derived porous carbons with high specific surface area  
399 and wide pore size distributions (including relatively high mesopore volumes), even at  
400 relatively low temperatures.

401

### 402 3.3. Catalytic activity

403 Due to their relatively high specific surface area, both PB\_700\_1.00 and CB\_3\_0.10  
404 activated biochars (one for each activation procedure) were selected as catalysts and tested  
405 during the upgrading process of the aqueous phase of a real pyrolysis oil.

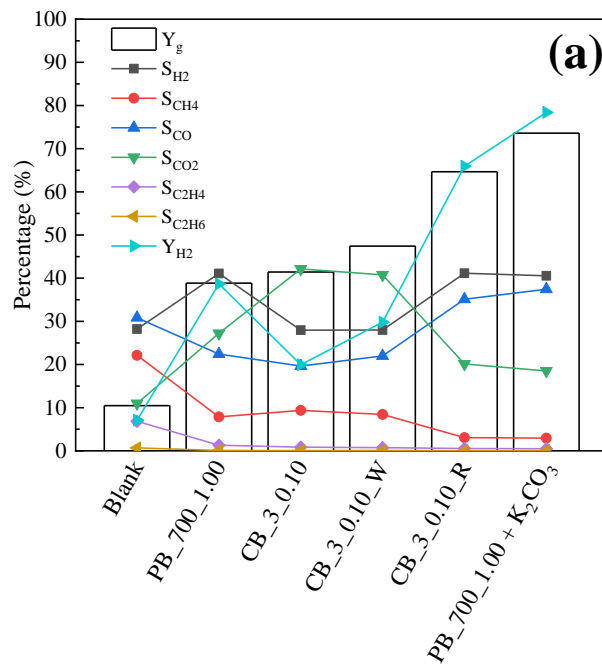
406 Elemental and moisture analyses of the aqueous phase of the pyrolysis oil revealed that the  
407 liquid sample had an average chemical formula of  $C_5H_{6.7}O_2$  and a water content of 80 wt. %.  
408 Since the liquid was fed to the reformer without providing additional water, the steam to  
409 carbon molar ratio, S:C, was 4:1.

410 It is generally assumed that deactivation and/or instability of the catalyst can be attributed  
411 to two different phenomena: (1) the deposition of carbonaceous material (coke) on the  
412 surface of the catalyst, which clogs part of the available active sites; and (2) the extent of  
413 gasification reactions (both with steam and  $CO_2$ ) of the carbon-based catalyst, which leads to  
414 a loss of mass and a subsequent increase in LHSV (i.e., less contact time).

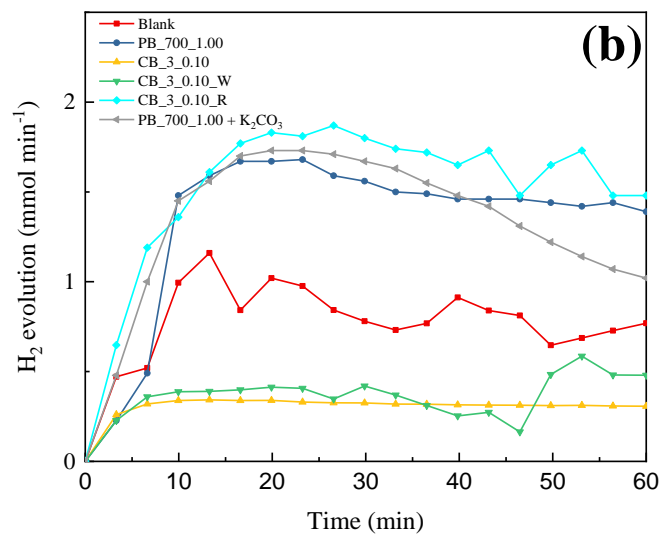
415 The results obtained in terms of total gas yield, selectivity towards specific gaseous  
416 species, hydrogen yield and hydrogen release over time are displayed in Fig. 3a. It should be  
417 noted that the poor results measured for the blank test (i.e., empty reactor) suggested that the  
418 reactor wall did not play a crucial catalytic role. The physically activated biochar  
419 (PB\_700\_1.00) exhibited performances comparable to those obtained in a previous study  
420 [33]. Using this material, which showed a good stability during the whole experiment (see  
421 Fig. 3b), a total gas yield of about 40% was obtained. Nevertheless, its relatively low  
422 hydrogen yield indicates that the extent of steam reforming was modest.

423 Regarding the performance of the chemically activated biochar (CB\_3\_0.10), a similar  
424 total gas yield was measured, compared to the physically activated one. However, selectivity  
425 to gaseous products were markedly different, leading to a decrease in the production of  $H_2$   
426 (the hydrogen yield was even lower than that of PB\_700\_1.00) and an increase in that of

427 CO<sub>2</sub>. This result could suggest that the decomposition of pyrolysis oil instead of steam and/or  
 428 dry reforming, was the main process involved.



429



430

431 **Fig. 3.** Results obtained from combined steam and dry reforming of pyrolysis oil at 750°C:  
 432 total and H<sub>2</sub> yields ( $Y_g$  and  $Y_{H_2}$ , respectively) as well as selectivities toward a given gaseous  
 433 product,  $S_i$  (a); and evolution of the hydrogen production rate (b).

434 As can be deduced from Fig. 3a, similar results were also obtained for the chemically  
 435 activated biochar that was washed with just water (CB\_3\_0.10\_W). The differences in the



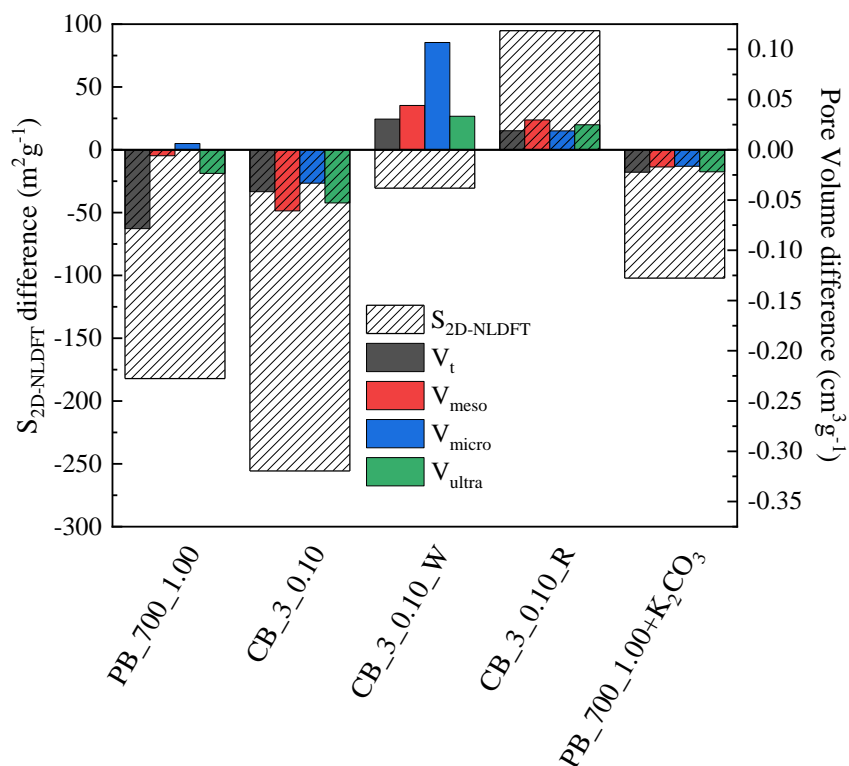
436 performance between the physically and chemically activated biochars could be related to  
437 their textural properties. In this respect, the physically activated biochar exhibited a higher  
438 specific surface area and higher volumes of micro- and mesopores, thus providing more  
439 catalytic active sites of inherent alkali or alkaline earth metal species (AAEMs). The catalytic  
440 role of these species (especially K, Mg and Ca) in both steam reforming and gasification of  
441 carbon has been widely reported [25,44–46]. Furthermore, the more hierarchical pore size  
442 distribution of PB\_700\_1.00, with relatively high contributions of the mesopores, could  
443 shorten the diffusion path to reach the active sites.

444 Fig. 3b clearly shows that H<sub>2</sub> release rates fluctuated over time for most of biochars tested.  
445 There are at least two possible explanations for this: First, the coke deposits, which gradually  
446 covered the catalyst surface, could have led to large fluctuations in the extent of the reactions  
447 involved. Second, the structural modification of the activated carbons (the process  
448 temperature was higher than the activation temperature) could also lead to unsteady hydrogen  
449 flow rates at the outlet. It should be noted that the reaction system studied was certainly  
450 complex, due to the numerous competitive reactions that can affect the yields of the different  
451 gaseous products. Nevertheless, it can be assumed that methane is mainly produced by the  
452 cracking of the heaviest fraction of the pyrolysis oil, and that its yield will be correlated to the  
453 amount of coke produced [47]. Similarly, Fig. 3a reveals that the selectivity towards methane  
454 was almost constant for PB\_700\_1.00, CB\_3\_0.10, and CB\_3\_0.10\_W materials. Therefore,  
455 it can be concluded that the coke production in the process was quite similar for the above-  
456 mentioned carbons, suggesting that some structural modifications in the carbons could be  
457 accounted for the unsteady production of hydrogen. These modifications could be ascribed to  
458 the reverse Boudouard reaction [48,49], steam gasification and, in the case of the chemical  
459 activated biochars, potassium-catalyzed gasification. To support this argument, Fig. 4 shows  
460 the textural properties of fresh and spent activated biochars. Contrary to the loss of porosity

461 observed for spent PB\_700\_1.00 and CB\_3\_0.10 catalysts, the spent CB\_3\_0.1\_W material  
462 showed an increase in pore volumes, especially for micropores. In addition, the results from  
463 TPD measurements, which are summarized graphically in Figs. 5 and A.6, indicate that the  
464 water-washed chemically activated carbon exhibited a larger mass loss (with an increased  
465 release of CO<sub>2</sub> and CO, as shown in Fig. A.6) than that of the acid-washed carbon, thus  
466 confirming a greater extent of carbon gasification. This fact could be attributed to the residual  
467 amount of activation reagent available on the surface of the catalyst CB\_3\_0.10\_W, which  
468 might promote further biochar gasification during the experiment, as recently reported by  
469 Wang *et al.* [11].

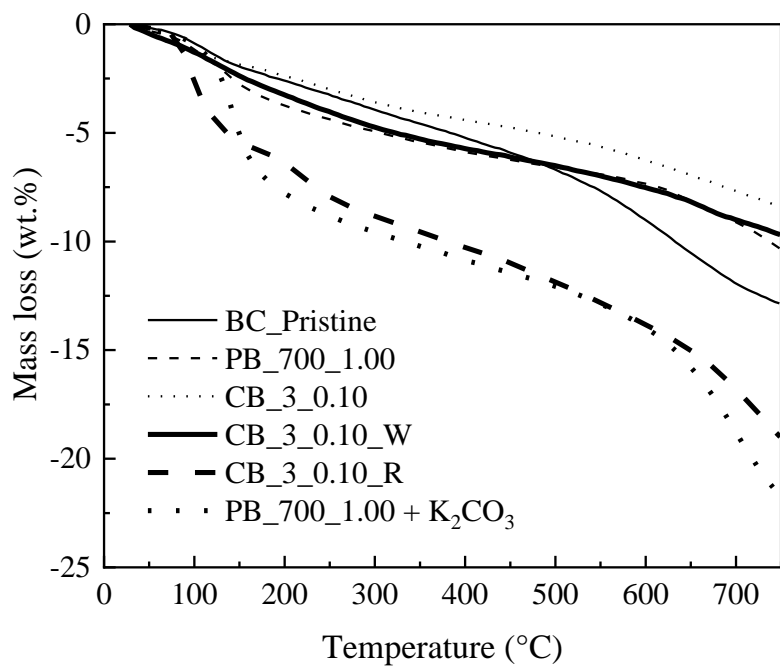
470 To understand better the effect of the washing procedure on the performance of  
471 chemically activated biochars, an unwashed (raw) material (CB\_3\_0.10\_R) was also tested as  
472 catalyst. In this case, the total gas yield was 65% with enhanced selectivity towards both H<sub>2</sub>  
473 and CO (see Fig. 3a), thus indicating a higher extent of the steam reforming reactions  
474 (leading to a  $Y_{H_2}$  of 66%). Fig. 6 displays the FTIR spectra obtained for fresh and spent  
475 chemically activated biochars as well as for pure K<sub>2</sub>CO<sub>3</sub>. In the case of acid and water-  
476 washed samples, no evident K<sub>2</sub>CO<sub>3</sub> content was detected on the surface, indicating the  
477 effectiveness of both washing procedures. On the other hand, most of the chemical activating  
478 agent available on the surface of the fresh CB\_3\_0.10\_R catalyst disappeared after the  
479 catalytic test. The potassium carbonate (and other chemical species derived from its partial  
480 decomposition) available on the surface of the catalyst at the beginning of the reforming test  
481 (reductive environment) could progressively be reduced to metallic potassium (K<sup>0</sup>), leading  
482 to a further promotion of reforming reactions. Furthermore, a process temperature relatively  
483 close to the volatilization point of potassium can enhance the mobility and reactivity of the  
484 metal [50]. Generally speaking, activated biochars have relatively abundant oxygen and  
485 nitrogen-containing functional groups, which are not present in the materials shown in Fig. 6.

486 The reason behind this could be the relatively high activation temperatures, since the majority  
 487 of functional groups decompose below 800 °C [51]. Furthermore, the relatively high amount  
 488 of  $K_2CO_3$  loaded on the analyzed samples resulted in a very large peak, which may hide other  
 489 peaks of interest, such as those related to oxygenated functionalities.



490  
 491 **Fig. 4.** Differences in textural properties between the fresh and spent activated biochars used  
 492 as catalysts in steam and dry reforming tests.

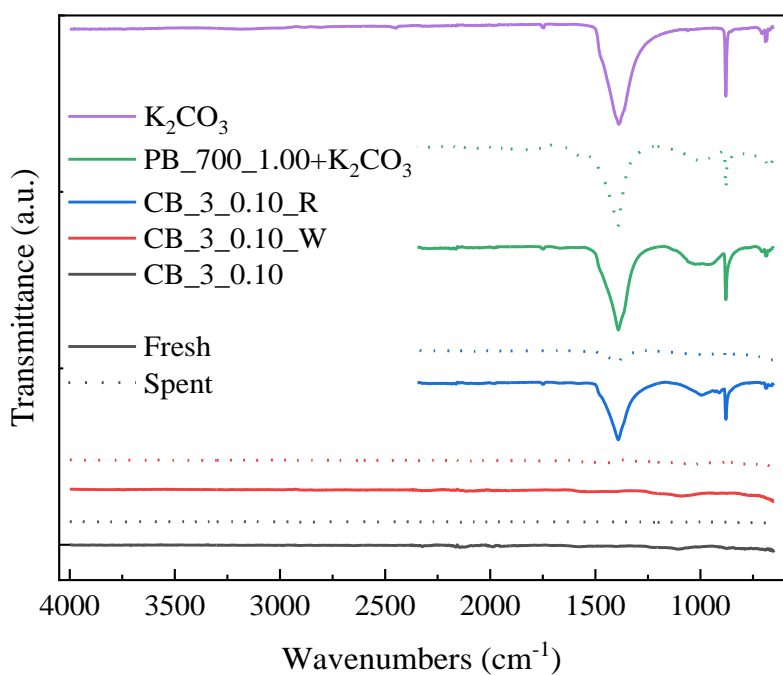
493



494

495 **Fig. 5.** Results from TPD characterization (percentage of mass loss vs. temperature) for

496 pristine and activated biochars.



497

498 **Fig. 6.** Comparison of the FTIR spectra obtained for pure  $K_2CO_3$  and some activated biochars

499 tested in the present study.

500 The results from TPD measurements (see Fig. 5) showed that the mass loss under an inert  
501 atmosphere was much higher for the unwashed catalyst. In addition, the release of CO during  
502 TPD also increased for the material CB\_3\_0.10\_R (see Fig. A.6c). The increase in both mass  
503 loss and CO production when heating in N<sub>2</sub> up to 750 °C could be due to the reaction of  
504 K<sub>2</sub>CO<sub>3</sub> with carbon, which results in an additional release of CO, especially at temperatures  
505 near 700 °C and above, and the formation of catalytically active COK and CK complexes  
506 [52]. Hence, a certain gasification of carbon during the catalytic upgrading tests should be  
507 expected. In line with this, Fig.4 shows that the spent CB\_3\_0.10\_R exhibited more  
508 developed textural properties than the fresh one (for instance, the specific surface area  
509 increased from 29 m<sup>2</sup> g<sup>-1</sup> to 124 m<sup>2</sup> g<sup>-1</sup>), thus confirming the extent of gasification reactions.  
510 Despite the loss of catalyst through carbon gasification, which results in a higher LHSV, the  
511 production rate of H<sub>2</sub> for this catalyst was relatively stable during the experiment. This could  
512 be explained by the fact that the carbon gasification catalyzed by K<sub>2</sub>CO<sub>3</sub> contributes to  
513 creating new pores and then counterbalancing the deposition of coke, which induces  
514 micropore blockage and active sites coverage.

515 Based on the findings discussed above, it seems reasonable to assume that an activated  
516 biochar having a wider hierarchical pore size distribution and some availability of K<sub>2</sub>CO<sub>3</sub> on  
517 its surface appears as an excellent candidate for catalytic pyrolysis vapors upgrading. With  
518 this in mind, a new biochar-derived material, designated as PB\_700\_1.00+K<sub>2</sub>CO<sub>3</sub>, was  
519 prepared by impregnating the material PB\_700\_1.00 with K<sub>2</sub>CO<sub>3</sub> at a mass ratio of carbonate  
520 to precursor of 3:1. It should be expected that the better textural properties of the starting  
521 physically activated biochar could lead to a more homogeneous dispersion of the active phase  
522 on the carbon support, thus resulting in an improved performance of the catalyst.

523 The results obtained for the catalyst PB\_700\_1.00+K<sub>2</sub>CO<sub>3</sub> confirmed our expectation. The  
524 total gas yield reached a maximum value of 74%, whereas the hydrogen yield was the highest

525 reported in the present study (78%). From the FTIR spectra given in Fig. 6, it can be seen that  
526 a fraction of  $K_2CO_3$  was still present on the catalyst surface after running the test.

527 XPS analyses were carried out for both PB\_700\_1.00 and PB\_700\_1.00+ $K_2CO_3$  materials  
528 to get additional insight into the role of  $K_2CO_3$  during the pyrolysis vapors upgrading  
529 process. From the summarized XPS results given in Table 4, it can be observed that the  
530 atomic composition of PB\_700\_1.00 remained relatively constant after the catalytic test, even  
531 though the simultaneous increase of the peaks related to CII and OII seemed to indicate the  
532 formation of phenolic groups on the catalysts. The comparison of the atomic compositions  
533 between the fresh and spent PB\_700\_1.00+ $K_2CO_3$  materials indicates that the extent of  
534 carbon gasification reactions was much higher than that of the PB\_700\_1.00 material.  
535 Furthermore, from the spectra displayed in Fig. A.7, an additional peak at 283 eV, which is  
536 attributed to  $KC_x$  carbides, was observed for the spent PB\_700\_1.00+ $K_2CO_3$ . On the other  
537 hand, the  $K2p_{3/2}$  region presented only a contribution and suggested the presence of  
538 potassium on the surface as  $K_2O$  or  $K_2O_2$ , according to Li *et al.*[53]. This fact was also  
539 confirmed by the shift to lower binding energies of the OII and OIII peaks (see Fig. A.7). The  
540 marked difference in the potassium content between fresh and spent PB\_700\_1.00+ $K_2CO_3$   
541 was probably due to the migration of the potassium-based compounds from the internal pores  
542 to the external surface, which can lead to the formation of a coating layer composed of  $K_2O$ ,  
543 as confirmed by SEM-EDX images reported in Fig. 7. The presence of potassium oxides on  
544 the surface of the catalyst can be ascribed to (i) the direct decomposition of the carbonate  
545 (Reaction 7) and/or (ii) the formation of metallic potassium. The latter can migrate from the  
546 inner structure of the catalyst to its surface during the course of the pyrolysis vapors  
547 upgrading tests and finally be oxidized when the catalyst has been removed from the reactor.  
548 This fact can also justify the significant decrease in the specific surface area reported in Fig. 4  
549 for the spent PB\_700\_1.00+ $K_2CO_3$  catalyst (from 130 to  $27.7\text{ m}^2\text{g}^{-1}$ ).

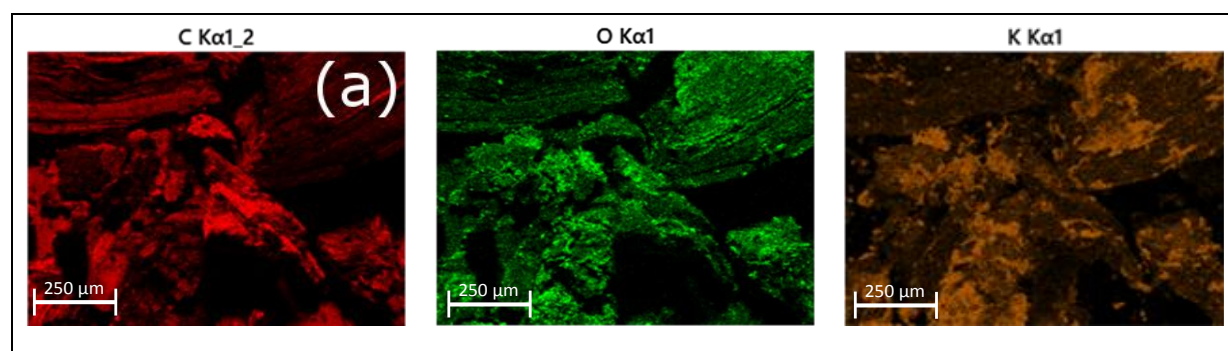
550 From the SEM-EDX analyses, it can also be deduced that a relatively homogeneous  
 551 dispersion of  $K_2CO_3$  was achieved for the fresh catalyst. Nevertheless, both fresh and spent  
 552 catalysts exhibited some clusters and snail shell-like agglomerates, which could be attributed  
 553 to the relatively high load of carbonate. However, no visible surface carbon layers was found  
 554 on the superficial  $K_2O$  of the spent catalyst, thus suggesting that the extent of the carbon  
 555 gasification was probably sufficient to prevent the deposition of coke on the surface.

556 **Table 4.** Surface composition measured by XPS and peak contributions of C1s, O1s and  
 557 K2p.

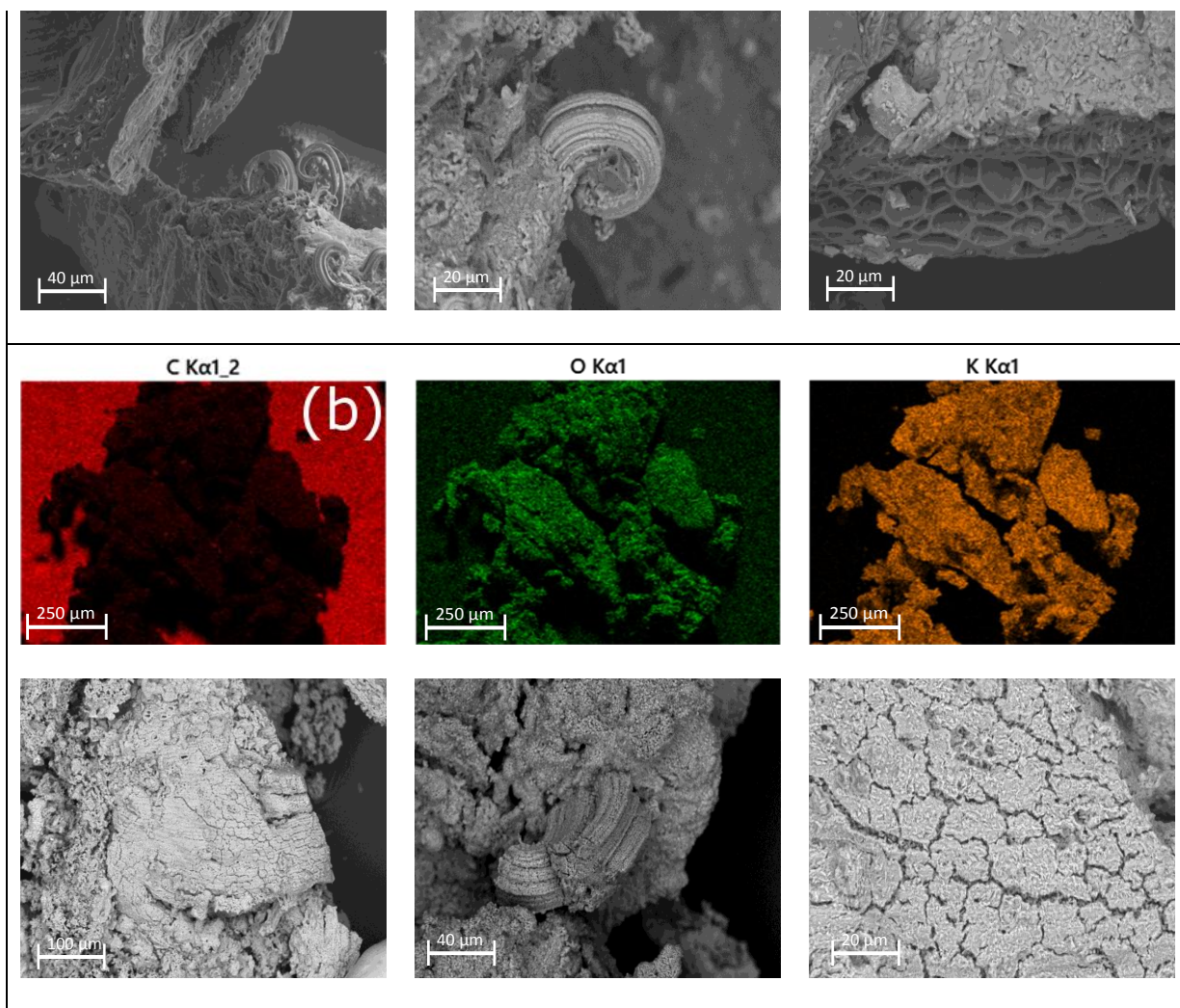
Sample	Surface concentration (at. %)			Binding energies (eV) and relative peak areas (%) <sup>e</sup>								
	C	O	K	CI	CII	CIII	CIV	Carbide	OI	OII	OIII	K2p3/2 region
PB_700_1.00 (Fresh)	87.3	11.3	1.4	284.4 (68.5)	285.7 (23.8)	287.6 (6.3)	289.2 (1.3)		531.1 (30.7)	532.8 (55.4)	534.5 (13.9)	293.3 (100)
PB_700_1.00 (Spent)	82.8	15.1	2.1	284.5 (62.7)	285.5 (31.3)	287.6 (4.1)	289.4 (1.9)		531.3 (20.0)	532.9 (60.2)	534.5 (19.8)	293.7 (100)
PB_700_1.00+ $K_2CO_3$ (Fresh)	72.6	21.6	5.8	284.6 (47.3)	285.8 (40.6)	287.6 (11.0)	289.3 (1.1)		531.3 (12.0)	532.7 (50.5)	534.5 (37.5)	293.7 (100)
PB_700_1.00+ $K_2CO_3$ (Spent)	42.0	27.8	30.2	284.5 (64.2)			288.7 (22.5)	283.1 (22.5)	531.1 (57.9)			292.8 (100)

558 <sup>e</sup> C1s binding energies in carbon materials: **CI**, hydrocarbons, aromatics, aliphatics (284.5 eV); **CII**, single bond  
 559 C-O associated to alcohols, phenols, carboxyls (286 eV); **CIII**, double bond C=O in carbonyl, quinone (287.5  
 560 eV); **CIV**, carboxyl and carbonate groups (288.7 eV).

561 O1s binding energies in carbon materials: **OI**, C=O quinone type groups (around 531 eV); **OII**, C-OH phenol  
 562 groups and/or C-O-C ether groups (532.5 eV), **OIII**, chemisorbed oxygen (COOH carboxylic groups) and/or



563 water (535 eV).



564 **Fig. 7.** SEM-EDX images of fresh (a) and spent (b) PB\_700\_1.00+K<sub>2</sub>CO<sub>3</sub> catalyst.

565 **4. Conclusions**

566 From the results obtained in this study, the following conclusions can be drawn:

- 567 1. The chemical activation of the pristine biochar led to carbonaceous solids with a  
 568 relatively high specific surface area and well-developed microporous structure.  
 569 The most important activation parameter was found to be the amount of activation  
 570 agent, which accounted for the development of the porous structure. Activation  
 571 pressure, on the other hand, was not significant for the outcomes of the procedure.  
 572 Regarding the washing efficiency, acid washing resulted to be effective in  
 573 cleaning the surface of the samples, whereas washing with water was not



574 sufficient to remove completely the residual reactants, partially clogging the  
575 porosity of the samples.

576 2. Physical activation was found to be more sensitive to the process parameters. It  
577 was possible to obtain acceptable values of specific surface area even at low  
578 temperature (650 °C) by increasing the activation pressure to 1.00 MPa. A  
579 negative effect of the activation temperature on the results was also observed. In  
580 fact, the surface area decreased with the increase in the activation temperature,  
581 probably due to the widening of the smaller pores by a too rapid (and thus less  
582 controlled) gasification.

583 3. The most promising material produced by physical or chemical activation  
584 (PB\_700\_1.00 and CB\_3\_0.10) were tested as catalysts in the upgrading of the  
585 aqueous fraction of a real pyrolysis oil. Both activated biochars, which were  
586 initially characterized by a well-developed porosity, did not exhibit good  
587 performance, showing a huge decrease in the specific surface area, probably due  
588 to coke deposition. Nevertheless, the addition of  $K_2CO_3$  to the best physically  
589 activated biochar boosted the overall performance towards the production of more  
590 hydrogen, as a consequence of the enhanced reforming of pyrolysis oil. This  
591 finding can be related to the availability of  $K^0$ , which was formed from the  
592 decomposition of the  $K_2CO_3$  previously deposited on the activated biochar.

593

## 594 **Acknowledgments**

595 This project received funding from the European Union's Horizon 2020 research and  
596 innovation programme under the Marie Skłodowska-Curie grant agreement No 721991. The  
597 authors also acknowledge the funding from the Aragón Government (Ref. T22\_20R), co-  
598 funded by FEDER 2014-2020 "Construyendo Europa desde Aragón". ". This study was  
599 partly supported by the French PIA project "Lorraine Université d'Excellence", reference  
600 ANR-15-IDEX-04-LUE, PROMOTEE project and TALiSMAN project, funded by FEDER  
601 (2019-000214). The authors gratefully thank José Antonio Manso (UNIZAR) and Philippe  
602 Gadonneix (IJL) for their help in the preparation and characterization of the samples and  
603 Sandrine Mathieu (IJL) for the SEM characterization.

## 604 **Appendix A. Supplementary data**

605 Further details on characterization of pristine and activated biochars. Statistical outcomes  
606 from the adopted designs of experiments.

## 607 **Nomenclature**

608	$A_{BET}$	Brunauer-Emmett-Teller area ( $\text{m}^2 \text{g}^{-1}$ )
609	$d_p$	Pore diameter (nm)
610	$F_{BO}$	Molar flow rate of dry bio oil ( $\text{mol min}^{-1}$ )
611	$F_{H2 Av}$	Experimental average $\text{H}_2$ molar flow rate ( $\text{mol min}^{-1}$ )
612	$F_{H2 Stoi}$	$\text{H}_2$ stoichiometric molar flow rate ( $\text{mol min}^{-1}$ )
613	$m_0$	Initial mass of biochar before activation (g)
614	$m_c$	Biochar mass before the washing step (g)
615	$m_f$	Final mass of biochar after activation (g)

616	$m_g$	Total mass of produced gas during the upgrading process (g)
617	$m_l$	Mass of liquid fed into the upgrading reactor (g)
618	$m_w$	Biochar mass after the washing step (g)
619	$n_i$	Produced amount of a given gaseous specie $i$ (mol)
620	$n_{tot}$	Total amount of produced gas (mol)
621	$S_{2D-NLDFT}$	2D-NLDFT specific surface area ( $m^2 g^{-1}$ )
622	$S_i$	Selectivity toward a given gaseous specie $i$ (%)
623	$V_{0.97}$	Gurvitch pore volume ( $cm^3 g^{-1}$ )
624	$V_{meso}$	Volume of mesopores ( $cm^3 g^{-1}$ )
625	$V_{micro}$	Volume of micropores ( $cm^3 g^{-1}$ )
626	$V_t$	Total pore volume ( $cm^3 g^{-1}$ )
627	$V_{ultra}$	Volume of ultra-micropores ( $cm^3 g^{-1}$ )
628	$Y_g$	Total gas yield (%)
629	$Y_{H2}$	Hydrogen yield (%)
630	$Y_{wash}$	Washing yield (%)
631	$\eta$	Degree of burnout (%)
632	<i>Acronyms</i>	
633	FTIR	Fourier-Transform Infrared spectroscopy
634	GHSV	Gas hourly space velocity
635	LHSV	Liquid hourly space velocity

636	PSD	Pore size distribution
637	RSM	Response surface methodology
638	S:C	Steam to carbon molar ratio
639	STP	Standard temperature and pressure
640	TPD	Temperature-programmed desorption
641	XPS	X-ray photoelectron spectroscopy
642	$\mu$ -GC	Micro gas chromatograph
643		

644 **References**

- 645 [1] Guedidi H, Lakehal I, Reinert L, Lévêque JM, Bellakhal N, Duclaux L. Removal of  
646 ionic liquids and ibuprofen by adsorption on a microporous activated carbon: Kinetics,  
647 isotherms, and pore sites. *Arab J Chem* 2020;13:258–70.  
648 <https://doi.org/10.1016/j.arabjc.2017.04.006>.
- 649 [2] Santoyo-Cisneros R, Rangel-Mendez JR, Nava JL, Larios-Durán ER, Chazaro-Ruiz  
650 LF. Influence of surface chemistry of activated carbon electrodes on electro-assisted  
651 adsorption of arsenate. *J Hazard Mater* 2020;392:122349.  
652 <https://doi.org/10.1016/j.jhazmat.2020.122349>.
- 653 [3] Acharya SP, Johnson J, Weidhaas J. Adsorption kinetics of the herbicide safeners,  
654 benoxacor and furilazole, to activated carbon and agricultural soils. *J Environ Sci*  
655 (China) 2020;89:23–34. <https://doi.org/10.1016/j.jes.2019.09.022>.
- 656 [4] Palomo J, Rodríguez-Cano MA, Rodríguez-Mirasol J, Cordero T. On the kinetics of  
657 methanol dehydration to dimethyl ether on Zr-loaded P-containing mesoporous  
658 activated carbon catalyst. *Chem Eng J* 2019;378:122198.  
659 <https://doi.org/10.1016/j.cej.2019.122198>.
- 660 [5] Liu WJ, Jiang H, Yu HQ. Development of Biochar-Based Functional Materials:  
661 Toward a Sustainable Platform Carbon Material. *Chem Rev* 2015;115:12251–85.  
662 <https://doi.org/10.1021/acs.chemrev.5b00195>.
- 663 [6] Wang Y, Yang H, Jin L, Li Y, Hu H, Ding H, et al. Effect of mineral in coal on  
664 preparation of activated carbon for methane decomposition to hydrogen. *Fuel*  
665 2019;258:116138. <https://doi.org/10.1016/j.fuel.2019.116138>.
- 666 [7] Li H, Zheng F, Wang J, Zhou J, Huang X, Chen L, et al. Facile preparation of zeolite-  
667 activated carbon composite from coal gangue with enhanced adsorption performance.  
668 *Chem Eng J* 2020;390:124513. <https://doi.org/10.1016/j.cej.2020.124513>.

- 669 [8] Ding S, Liu Y. Adsorption of CO<sub>2</sub> from flue gas by novel seaweed-based KOH-  
670 activated porous biochars. *Fuel* 2020;260:116382.  
671 <https://doi.org/10.1016/j.fuel.2019.116382>.
- 672 [9] Iriarte-Velasco U, Sierra I, Zudaire L, Ayastuy JL. Preparation of a porous biochar  
673 from the acid activation of pork bones. *Food Bioprod Process* 2016;98:341–53.  
674 <https://doi.org/10.1016/j.fbp.2016.03.003>.
- 675 [10] Saygılı H, Akkaya Saygılı G. Optimized preparation for bimodal porous carbon from  
676 lentil processing waste by microwave-assisted K<sub>2</sub>CO<sub>3</sub> activation : Spectroscopic  
677 characterization and dye decolorization activity. *J Clean Prod* 2019;226:968–76.  
678 <https://doi.org/10.1016/j.jclepro.2019.04.121>.
- 679 [11] Wang L, Sun F, Hao F, Qu Z, Gao J, Liu M, et al. A green trace K<sub>2</sub>CO<sub>3</sub> induced  
680 catalytic activation strategy for developing coal-converted activated carbon as  
681 advanced candidate for CO<sub>2</sub> adsorption and supercapacitors. *Chem Eng J*  
682 2020;383:123205. <https://doi.org/10.1016/j.cej.2019.123205>.
- 683 [12] Mai TT, Vu DL, Huynh DC, Wu NL, Le AT. Cost-effective porous carbon materials  
684 synthesized by carbonizing rice husk and K<sub>2</sub>CO<sub>3</sub> activation and their application for  
685 lithium-sulfur batteries. *J Sci Adv Mater Devices* 2019;4:223–9.  
686 <https://doi.org/10.1016/j.jsamd.2019.04.009>.
- 687 [13] Lahijani P, Zainal ZA, Mohammadi M, Mohamed AR. Conversion of the greenhouse  
688 gas CO<sub>2</sub> to the fuel gas CO via the Boudouard reaction: A review. *Renew Sustain*  
689 *Energy Rev* 2015;41:615–32. <https://doi.org/10.1016/j.rser.2014.08.034>.
- 690 [14] Şahin Ö, Saka C. Preparation and characterization of activated carbon from acorn shell  
691 by physical activation with H<sub>2</sub>O – CO<sub>2</sub> in two-step pretreatment. *Bioresour Technol*  
692 2013;136:163–8. <https://doi.org/10.1016/j.biortech.2013.02.074>.
- 693 [15] Guo Y, Tan C, Sun J, Li W, Zhang J, Zhao C. Porous activated carbons derived from

- 694 waste sugarcane bagasse for CO<sub>2</sub> adsorption. Chem Eng J 2020;381:122736.  
695 <https://doi.org/10.1016/j.cej.2019.122736>.
- 696 [16] Bertero M, Puente G De, Sedran U. Fuels from bio-oils : Bio-oil production from  
697 different residual sources , characterization and thermal conditioning. Fuel  
698 2012;95:263–71. <https://doi.org/10.1016/j.fuel.2011.08.041>.
- 699 [17] Fu M, Qi W, Xu Q, Zhang S, Yan Y. Hydrogen production from bio-oil model  
700 compounds dry ( CO<sub>2</sub>) reforming over Ni/Al<sub>2</sub>O<sub>3</sub> catalyst. Int J Hydrogen Energy  
701 2015;41:1494–501. <https://doi.org/10.1016/j.ijhydene.2015.11.104>.
- 702 [18] Santamaria L, Artetxe M, Lopez G, Cortazar M, Amutio M, Bilbao J, et al. Effect of  
703 CeO<sub>2</sub> and MgO promoters on the performance of a Ni/Al<sub>2</sub>O<sub>3</sub> catalyst in the steam  
704 reforming of biomass pyrolysis volatiles. Fuel Process Technol 2020;198:106223.  
705 <https://doi.org/10.1016/j.fuproc.2019.106223>.
- 706 [19] Santamaria L, Lopez G, Arregi A, Amutio M, Artetxe M, Bilbao J, et al. Stability of  
707 different Ni supported catalysts in the in-line steam reforming of biomass fast  
708 pyrolysis volatiles. Appl Catal B Environ 2019;242:109–20.  
709 <https://doi.org/10.1016/j.apcatb.2018.09.081>.
- 710 [20] Bimbela F, Ábrego J, Puerta R, García L, Arauzo J. Catalytic steam reforming of the  
711 aqueous fraction of bio-oil using Ni-Ce / Mg-Al catalysts. Appl Catal B Environ  
712 2017;209:346–57. <https://doi.org/10.1016/j.apcatb.2017.03.009>.
- 713 [21] Phongprueksathat N, Meeyoo V, Rirksomboon T. Steam reforming of acetic acid for  
714 hydrogenproduction : Catalytic performances of Ni and Co supported on  
715 Ce<sub>0.75</sub>Zr<sub>0.25</sub>O<sub>2</sub> catalysts. Int J Hydrogen Energy 2019;44:9359–67.  
716 <https://doi.org/10.1016/j.ijhydene.2019.02.085>.
- 717 [22] Domine ME, Iojoiu EE, Davidian T, Guillaume N, Mirodatos C. Hydrogen production  
718 from biomass-derived oil over monolithic Pt- and Rh-based catalysts using steam

- 719 reforming and sequential cracking processes. *Catal Today* 2008;133–135:565–73.  
720 <https://doi.org/10.1016/j.cattod.2007.12.062>.
- 721 [23] Li X, Zhang Z, Zhang L, Fan H, Li X, Liu Q, et al. Investigation of coking behaviors  
722 of model compounds in bio-oil during steam reforming. *Fuel* 2020;265:116961.  
723 <https://doi.org/10.1016/j.fuel.2019.116961>.
- 724 [24] Ma Z, Xiao R, Zhang H. Catalytic steam reforming of bio-oil model compounds for  
725 hydrogen-rich gas production using bio-char as catalyst. *Int J Hydrogen Energy*  
726 2016;42:3579–85. <https://doi.org/10.1016/j.ijhydene.2016.11.107>.
- 727 [25] Feng D, Zhao Y, Zhang Y, Sun S, Meng S, Guo Y, et al. Effects of K and Ca on  
728 reforming of model tar compounds with pyrolysis biochars under H<sub>2</sub>O or CO<sub>2</sub>. *Chem*  
729 *Eng J* 2016;306:422–32. <https://doi.org/10.1016/j.cej.2016.07.065>.
- 730 [26] Buentello-Montoya D, Zhang X, Li J, Ranade V, Marques S, Geron M. Performance  
731 of biochar as a catalyst for tar steam reforming: Effect of the porous structure. *Appl*  
732 *Energy* 2020;259:114176. <https://doi.org/10.1016/j.apenergy.2019.114176>.
- 733 [27] Feng D, Zhao Y, Zhang Y, Zhang Z, Sun S. Roles and fates of K and Ca species on  
734 biochar structure during in-situ tar H<sub>2</sub>O reforming over nascent biochar. *Int J*  
735 *Hydrogen Energy* 2017;42:21686–96. <https://doi.org/10.1016/j.ijhydene.2017.07.096>.
- 736 [28] Zhang Z, Ou Z, Qin C, Ran J, Wu C. Roles of alkali/alkaline earth metals in steam  
737 reforming of biomass tar for hydrogen production over perovskite supported Ni  
738 catalysts. *Fuel* 2019;257:116032. <https://doi.org/10.1016/j.fuel.2019.116032>.
- 739 [29] Megaritis A, Zhuo Y, Messenböck R, Dugwell DR, Kandiyoti R. Pyrolysis and  
740 gasification in a bench-scale high-pressure fluidized-bed reactor. *Energy Fuels*  
741 1998;12:144–51. <https://doi.org/10.1021/ef970115x>.
- 742 [30] Dufour A, Celzard A, Fierro V, Martin E, Broust F, Zoulalian A. Catalytic  
743 decomposition of methane over a wood char concurrently activated by a pyrolysis gas.



- 744 Appl Catal A Gen 2008;346:164–73. <https://doi.org/10.1016/j.apcata.2008.05.023>.
- 745 [31] Ranguin R, Jean-Marius C, Yacou C, Gaspard S, Feidt C, Rychen G, et al. Reduction  
746 of chlordecone environmental availability by soil amendment of biochars and activated  
747 carbons from lignocellulosic biomass. Environ Sci Pollut Res 2020.  
748 <https://doi.org/10.1007/s11356-019-07366-2>.
- 749 [32] Greco G, Videgain M, Di Stasi C, González B, Manyà JJ. Evolution of the mass-loss  
750 rate during atmospheric and pressurized slow pyrolysis of wheat straw in a bench-scale  
751 reactor. J Anal Appl Pyrolysis 2018;136:18–26.  
752 <https://doi.org/10.1016/j.jaap.2018.11.007>.
- 753 [33] Di Stasi C, Alvira D, Greco G, González B, Manyà JJ. Physically activated wheat  
754 straw-derived biochar for biomass pyrolysis vapors upgrading with high resistance  
755 against coke deactivation. Fuel 2019;255:115807.  
756 <https://doi.org/10.1016/j.fuel.2019.115807>.
- 757 [34] Jagiello J, Kenvin J, Celzard A, Fierro V. Enhanced resolution of ultra micropore size  
758 determination of biochars and activated carbons by dual gas analysis using N<sub>2</sub> and  
759 CO<sub>2</sub> with 2D-NLDFT adsorption models. Carbon 2019;144:206–15.  
760 <https://doi.org/10.1016/j.carbon.2018.12.028>.
- 761 [35] Sanchez-Sanchez A, Izquierdo MT, Medjahdi G, Ghanbaja J, Celzard A, Fierro V.  
762 Ordered mesoporous carbons obtained by soft-templating of tannin in mild conditions.  
763 Microporous Mesoporous Mater 2018;270:127–39.  
764 <https://doi.org/10.1016/j.micromeso.2018.05.017>.
- 765 [36] Matos J, Labady M, Albornoz A, Laine J, Brito JL. Catalytic effect of KOH on  
766 textural changes of carbon macro-networks by physical activation. J Mol Catal A  
767 Chem 2005;228:189–94. <https://doi.org/10.1016/j.molcata.2004.09.039>.
- 768 [37] Lozano-Castelló D, Calo JM, Cazorla-Amorós D, Linares-Solano A. Carbon activation

769 with KOH as explored by temperature programmed techniques, and the effects of  
770 hydrogen. *Carbon* 2007;45:2529–36. <https://doi.org/10.1016/j.carbon.2007.08.021>.

771 [38] Ganga Devi T, Kannan MP. Calcium catalysis in air gasification of cellulosic chars.  
772 *Fuel* 1998;77:1825–30. [https://doi.org/10.1016/S0016-2361\(98\)00038-6](https://doi.org/10.1016/S0016-2361(98)00038-6).

773 [39] Dehkhoda AM, Gyenge E, Ellis N. A novel method to tailor the porous structure of  
774 KOH-activated biochar and its application in capacitive deionization and energy  
775 storage. *Biomass Bioenergy* 2016;87:107–21.  
776 <https://doi.org/10.1016/j.biombioe.2016.02.023>.

777 [40] Malekshahian M, Hill JM. Effect of pyrolysis and CO<sub>2</sub> gasification pressure on the  
778 surface area and pore size distribution of petroleum coke. *Energy Fuels* 2011;25:5250–  
779 6. <https://doi.org/10.1021/ef201231w>.

780 [41] Montané D, Fierro V, Marêché JF, Aranda L, Celzard A. Activation of biomass-  
781 derived charcoal with supercritical water. *Microporous Mesoporous Mater*  
782 2009;119:53–9. <https://doi.org/10.1016/j.micromeso.2008.09.040>.

783 [42] Malekshahian M, Hill JM. Kinetic Analysis of CO<sub>2</sub> Gasification of Petroleum Coke at  
784 High Pressures. *Energy Fuels* 2011;25:4043–8. <https://doi.org/10.1021/ef2009259>.

785 [43] Feroso J, Stevanov C, Moghtaderi B, Arias B, Pevida C, Plaza MG, et al. High-  
786 pressure gasification reactivity of biomass chars produced at different temperatures. *J*  
787 *Anal Appl Pyrolysis* 2009;85:287–93. <https://doi.org/10.1016/j.jaap.2008.09.017>.

788 [44] Yip K, Tian F, Hayashi JI, Wu H. Effect of alkali and alkaline earth metallic species  
789 on biochar reactivity and syngas compositions during steam gasification. *Energy Fuels*  
790 2010;24:173–81. <https://doi.org/10.1021/ef900534n>.

791 [45] Sueyasu T, Oike T, Mori A, Kudo S, Norinaga K, Hayashi JI. Simultaneous steam  
792 reforming of tar and steam gasification of char from the pyrolysis of potassium-loaded  
793 woody biomass. *Energy Fuels* 2012;26:199–208. <https://doi.org/10.1021/ef201166a>.

- 794 [46] Jiang L, Hu S, Wang Y, Su S, Sun L, Xu B, et al. Catalytic effects of inherent alkali  
795 and alkaline earth metallic species on steam gasification of biomass. *Int J Hydrogen*  
796 *Energy* 2015;40:15460–9. <https://doi.org/10.1016/j.ijhydene.2015.08.111>.
- 797 [47] Matos J, Laine J. Ethylene conversion on activated carbon-supported NiMo catalysts:  
798 Effect of the support. *Appl Catal A Gen* 2003;241:25–38.  
799 [https://doi.org/10.1016/S0926-860X\(02\)00427-1](https://doi.org/10.1016/S0926-860X(02)00427-1).
- 800 [48] Díaz K, García V, Matos J. Activated carbon supported Ni – Ca: Influence of reaction  
801 parameters on activity and stability of catalyst on methane reformation. *Fuel*  
802 2007;86:1337–44. <https://doi.org/10.1016/j.fuel.2006.05.011>.
- 803 [49] Matos J, Díaz K, García V, Cordero TC, Brito JL. Methane transformation in presence  
804 of carbon dioxide on activated carbon supported nickel – calcium catalysts. *Catalysis*  
805 *Lett.* 2006;109:163–169. <https://doi.org/10.1007/s10562-006-0073-3>.
- 806 [50] Ducouso M, Weiss-Hortala E, Lyczko N, Nzihou A, Castaldi MJ. 110th Anniversary:  
807 Syngas Production Enhancement Using Calcium- And Potassium-Impregnated Chars.  
808 *Ind Eng Chem Res* 2019;58:15134–41. <https://doi.org/10.1021/acs.iecr.9b02238>.
- 809 [51] Figueiredo JL, Pereira MFR. The role of surface chemistry in catalysis with carbons.  
810 *Catal Today* 2010;150:2–7. <https://doi.org/10.1016/j.cattod.2009.04.010>.
- 811 [52] Kopyscinski J, Rahman M, Gupta R, Mims CA, Hill JM. K<sub>2</sub>CO<sub>3</sub> catalyzed CO<sub>2</sub>  
812 gasification of ash-free coal. Interactions of the catalyst with carbon in N<sub>2</sub> and CO<sub>2</sub>  
813 atmosphere. *Fuel* 2014;117:1181–9. <https://doi.org/10.1016/j.fuel.2013.07.030>.
- 814 [53] Li X, Liu J, Kong F, Liu X, Xu J, Chen H. Potassium-doped graphene for  
815 simultaneous determination of nitrite and sulfite in polluted water. *Electrochem*  
816 *Commun* 2012;20:109–12. <https://doi.org/10.1016/j.elecom.2012.04.014>.
- 817